UNIVERSITY of York

This is a repository copy of *Impact of equilibrium radial electric field on energy loss process after pedestal collapse*.

White Rose Research Online URL for this paper:
https://eprints.whiterose.ac.uk/159576/

Version: Accepted Version

Article:
Seto, Haruki, Xu, X. Q., Dudson, Benjamin Daniel orcid.org/0000-0002-0094-4867 et al. (1 more author) (2020) Impact of equilibrium radial electric field on energy loss process after pedestal collapse. Contributions to plasma physics. e201900158. ISSN 0863-1042

https://doi.org/10.1002/ctpp.201900158

Reuse
Items deposited in White Rose Research Online are protected by copyright, with all rights reserved unless indicated otherwise. They may be downloaded and/or printed for private study, or other acts as permitted by national copyright laws. The publisher or other rights holders may allow further reproduction and re-use of the full text version. This is indicated by the licence information on the White Rose Research Online record for the item.

Takedown
If you consider content in White Rose Research Online to be in breach of UK law, please notify us by emailing eprints@whiterose.ac.uk including the URL of the record and the reason for the withdrawal request.

White Rose university consortium
Universities of Leeds, Sheffield & York

eprints@whiterose.ac.uk
https://eprints.whiterose.ac.uk/

Received <day> <Month>, <year>; | Revised <day> <Month>, <year>; | Accepted <day> <Month>, <year>

DOI: xxx/xxxx

ARTICLE TYPE

Impact of equilibrium radial electric field on energy loss process after pedestal collapse

Haruki Seto*[1] | Xueqiao Xu[2] | Benjamin D. Dudson[3] | Masatoshi Yagi[1]

[1] Rokkasho Fusion Institute, National Institutes for Quantum and Radiological Science and Technology, Aomori, Japan
[2]Lawrence Livermore National Laboratory, California, USA
[3]York Plasma Institute, Department of Physics, University of York, York, UK

Correspondence
*Haruki Seto, Rokkasho Fusion Institute, National Institutes for Quantum and Radiological Science and Technology, Aomori, Japan.
Email: seto.haruki@qst.go.jp

Present Address
2-166, Omotedate-Obuchi, Rokkasho-mura, Kamikita-gun, Aomori, Japan

Abstract

An impact of the equilibrium radial electric field on energy loss processes after the pedestal collapse is numerically investigated with the BOUT++ framework. Using linear stability analysis, the resistive ballooning mode (RBM) is shown to be stabilized by the radial shear of equilibrium radial electric field. On the other hand, the energy loss level after the pedestal collapse increases if the equilibrium radial electric field is taken into account. The spatio-temporal and phase diagram analyses show that the equilibrium radial electric field partially cancels the fluctuation driven toroidally axisymmetric radial electric field and weakens $E \times B$ shearing rate after pedestal collapse, weakening the turbulence suppression by vortex shearing. The equilibrium radial electric field therefore increases turbulence intensity in nonlinear cyclic oscillations among pressure gradient, $E \times B$ shearing rate and turbulence intensity, which gives rise to subsequent bursts of turbulent transport and increases energy loss level.

KEYWORDS:
pedestal collapse, radial electric field, nonlinear cyclic oscillations, reduced MHD model

1 | INTRODUCTION

The high-confinement mode discharge[1] is a baseline operation scenario in ITER[2] and DEMO fusion reactors[3] since the high energy amplification factor is important for economic viability. The intermittent large heat fluxes released by edge localized modes (ELMs)[4] however should be avoided or mitigated to a level low enough to remain within heat load constraints on plasma facing components. Nonlinear MHD codes such as JOREK[5,6], NIMROD[7], M3D-C1[8] and BOUT++[9–11] have therefore been developed and provided qualitative understandings of ELMs and their resultant energy loss processes.

Fluctuation driven toroidal axisymmetric ($n = 0$) flows, generally called convective cell modes[12] (CCs), and especially zonal flows[13] (ZFs) for ($m = 0, n = 0$) mode, affect energy loss processes during ELMs. It is reported that CCs suppress and also enhance energy loss by different mechanisms, where m and n are the poloidal and toroidal mode number respectively. For the energy loss suppression effect of CCs, JOREK simulation[5] reveals that the $E \times B$ shearing rate[14,15] of CCs generated by the residual of MHD force balance during the pedestal collapse suppress the filament transport. For the energy loss enhancement effect of CCs, on the other hand, BOUT++ simulation[16] shows that ZFs with geodesic acoustic modes (GAM)[17] driven by the residual of flow stress during the pedestal collapse drive secondary instabilities, which results in secondary small crashes after a large collapse like compound ELMs[18].

In previous BOUT++ studies including Ref.[16], there was a limitation on solving ($m \neq 0, n = 0$) component of vorticity equation and $n = 0$ component of Ohm's law due to the flute-ordered approximation in Poisson solver, which is explicitly mentioned in several papers[10,11]. This is because that the flute-ordered Poisson solver cannot reproduce ($m \neq 0, n = 0$)

component of the flow potential from the vorticity and ($m \neq 0, n = 0$) component of vorticity equation describing the MHD force balance is indispensable for self-consistent evolution of $n = 0$ magnetic field. The energy loss suppression by CCs generated by the residual of MHD force balance was therefore not taken into account in the previous BOUT++ results.

This numerical issue has been recently resolved by introducing a two-dimensional Poisson solver designed for $n = 0$ mode. This solver was originally developed for the flux-driven edge turbulence BOUT++ module Hermes[19] and has been modified for a BOUT++ ELM physics module[20]. In this framework, the CCs mainly generated by the residual of MHD force balance suppress energy loss during the pedestal collapse and the secondary instability accompanied with nonlinear damped oscillations among pressure gradient, $E \times B$ flow shear and turbulence intensity enhance energy loss in the late nonlinear phase[20].

However, the equilibrium radial electric field is neglected in our previous work, which means that the equilibrium radial force balance is not satisfied. In this paper, an impact of equilibrium radial electric field on energy loss by an interplay between $n = 0$ net flow and turbulence after the pedestal collapse is numerically investigated.

The remainder of this paper is organized as follows. Section 2 presents the four-field model including the equilibrium radial electric field and the shifted circular equilibrium. An impact of the equilibrium radial electric field on energy loss process after the pedestal collapse is reported in Sec. 3. Finally this paper is summarized in Sec. 4.

2 | FOUR-FIELD REDUCED MHD MODEL AND MHD EQUILIBRIUM

A scale separated four-field reduced MHD model describing peeling-ballooning modes with non-ideal effects including ion diamagnetism, electron drift wave, resistivity, hyper-resistivity, flow compression and mean radial electric field is employed. The model consists of equations for vorticity ϖ_1, magnetic potential $A_{\parallel 1}$, plasma pressure p_1 and ion parallel flow $v_{\parallel 1}$ as,

$$\frac{\partial}{\partial t}\varpi_1 = -\left[F_1, \varpi\right] - \left[F_0, \varpi_1\right] + \mathcal{G}\left(p_1, F\right) + \mathcal{G}\left(p_0, F_1\right) - B_0\partial_\parallel\left(\frac{J_{\parallel 1}}{B_0}\right) + B_0\left[A_{\parallel 1}, \frac{J_\parallel}{B_0}\right] + \mathcal{K}(p_1) + \mu_\parallel\partial_\parallel^2\varpi_1 + \mu_\perp\nabla_\perp^2\varpi_1, \quad (1)$$

$$\frac{\partial}{\partial t}p_1 = -\left[\phi_1, p\right] - \left[\phi_0, p_1\right] - 2\beta_*\left(\mathcal{K}(p_1) - B_0\partial_\parallel\left(\frac{v_{\parallel 1} + d_i J_{\parallel 1}}{2B_0}\right) + B_0\left[A_{\parallel 1}, \frac{v_{\parallel 1} + d_i J_{\parallel 1}}{2B_0}\right]\right) + \chi_\parallel\partial_\parallel^2 p_1 + \chi_\perp\nabla_\perp^2 p_1, \quad (2)$$

$$\frac{\partial}{\partial t}A_{\parallel 1} = -\left[\phi, A_{\parallel 1}\right] - \partial_\parallel\phi_1 + \delta_e\left(\partial_\parallel p_1 - \left[A_{\parallel 1}, p\right]\right) + \eta J_{\parallel 1} - \lambda\nabla_\perp^2 J_{\parallel 1}, \quad (3)$$

$$\frac{\partial}{\partial t}v_{\parallel 1} = -\left[\phi, v_{\parallel 1}\right] - \frac{1}{2}\left(\partial_\parallel p_1 - \left[A_{\parallel 1}, p\right]\right) + \nu_\perp\nabla_\perp^2 v_{\parallel 1}, \quad (4)$$

$$\varpi = \nabla_\perp^{*2}F, \quad J_1 = \nabla_\perp^2 A_\parallel, \quad F = \phi + \delta_i p, \quad \phi = \phi_0 + \phi_1, \quad p = p_0 + p_1, \quad \boldsymbol{B} = \boldsymbol{B}_0 + \nabla A_{\parallel 1}\times\boldsymbol{b}_0, \quad J_\parallel = J_{\parallel 0} + J_{\parallel 1},$$

where quantities with subscript 0 represent equilibrium components and those with subscript 1 represent perturbed components respectively. Here, $[f, g] = (\boldsymbol{b}_0\times\nabla f\cdot\nabla g)/B_0$, $\mathcal{G}(f, g) = \delta_i\left(\left[f, \nabla_\perp^{*2}g\right] + \left[g, \nabla_\perp^{*2}f\right] + \nabla_\perp^{*2}[f, g]\right)/2$, $\mathcal{K}(f) = (\boldsymbol{b}_0\times\boldsymbol{\kappa}_0\cdot\nabla f)/B_0$, $\partial_\parallel f = \boldsymbol{b}_0\cdot\nabla f$, $\nabla_\perp f = (\nabla - \boldsymbol{b}_0\partial_\parallel)f$, $\nabla_\perp^2 f = \nabla\cdot\nabla_\perp f$, $\nabla_\perp^{*2}f = \nabla\cdot[(\nabla_\perp f)/B_0]$ for any f and g, the unit vector along the equilibrium magnetic field line $\boldsymbol{b}_0 = \boldsymbol{B}_0/B_0$, the equilibrium magnetic field curvature $\boldsymbol{\kappa}_0 = \boldsymbol{b}_0\cdot\nabla\boldsymbol{b}_0$, the generalized flow potential F, the electrostatic potential ϕ, the parallel current $\boldsymbol{J}_\parallel$, the compression parameter $\beta_* = B_0^2/[0.5 + B_0^2/(5p_0/3)]$, the factor for ion diamagnetism $\delta_i = d_i/4$, the factor for electron diamagnetism $\delta_e = d_i/4$, the ion skin depth $d_i = (c/R_{\mathrm{ax}})\sqrt{(m_i\varepsilon_0)/(n_i Z_i^2 e^2)}$, the speed of light in vacuum c, the permeability in vacuum ϵ_0, the ion charge number Z_i, the elementary charge e, the parallel viscosity for vorticity $\mu_\parallel$, the perpendicular viscosity for vorticity $\mu_\perp$, the parallel diffusivity $\chi_\parallel$, the perpendicular diffusivity $\chi_\perp$, the resistivity η, the hyper resistivity λ and the perpendicular viscosity for ion parallel flow $\nu_\perp$ respectively.

The four-field model is normalized with poloidal Alfvén units with the plasma major radius at the magnetic axis R_{ax}, the magnetic field intensity at the magnetic field B_{ax} the reference ion number density n_i, and poloidal Alfvén time $t_A = R_{\mathrm{ax}}/V_A$. where $V_A = B_{\mathrm{ax}}/\sqrt{\mu_0 m_i n_i}$ is the Alfvén velocity, μ_0 is the permittivity in vacuum and m_i is the ion mass respectively. In the derivation of Eqs.(1)-(4), the iso-thermal approximation, the charge quasi-neutrality with $Z_i = 1$ and the Boussinesq approximation with a flat ion number density profile have been assumed. The equilibrium electrostatic potential designed to make the equilibrium $E \times B$ flow cancel with the equilibrium ion diamagnetic flow can be therefore expressed as $\phi_0 = -\delta_i p_0$, where the neoclassical poloidal flow and its return flow are not taken account in this work.

For the generation mechanism of $n = 0$ net flow, we derive the equation of $n = 0$ perpendicular kinetic energy $W_k^{n=0} = \langle|\nabla_\perp F_1^{n=0}|^2/(2B_0)\rangle_V$ by multiplying Eq.(1) by $n = 0$ generalized flow potential $-F_1^{n=0}$ and integrating it over the entire domain,

$$\frac{d}{dt}W_k^{n=0} = T_{k,R}^{n=0} + T_{k,ID}^{n=0} + T_{k,LB}^{n=0} + T_{k,K}^{n=0} + T_{k,M}^{n=0} + T_{k,C}^{n=0} + T_{k,D}^{n=0}. \quad (5)$$

In Eq. (5), $T^{n=0}_{k,R} = \langle F^{n=0}_1[F_0, \varpi_1]\rangle_V + \langle F^{n=0}_1[F_1, \varpi]\rangle_V$ is the change rate of $n = 0$ perpendicular kinetic energy by the Reynolds stress, $T^{n=0}_{k,ID} = -\langle F^{n=0}_1 \mathcal{G}(p_1, F)\rangle_V - \langle F^{n=0}_1 \mathcal{G}(p_0, F_1)\rangle_V$ by the ion diamagnetic stress, $T^{n=0}_{k,LB} = \langle F^{n=0}_1 B_0 \partial_\parallel \left(J_{\parallel 1}/B_0\right)\rangle_V$ by the line-bending force, $T^{n=0}_{k,K} = -\langle F^{n=0}_1 B_0 \left[A_{\parallel 1}, J_{\parallel 0}/B_0\right]\rangle_V$ by the kink term, $T^{n=0}_{k,M} = -\langle F^{n=0}_1 B_0 \left[A_{\parallel 1}, J_{\parallel 1}/B_0\right]\rangle_V$ by the Maxwell stress, $T^{n=0}_{k,C} = -\langle F^{n=0}_1 \mathcal{K}(p_1)\rangle_V$ by the toroidal curvature and $T^{n=0}_{k,D} = -\langle \mu_\parallel |\partial_\parallel F^{n=0}_1|^2\rangle_V - \langle \mu_\perp |\nabla_\perp F^{n=0}_1|^2\rangle_V$ by dissipation respectively. Here, $\langle f\rangle_V = \int_V f dV$ represents the volume integral over the entire domain.

A shifted circular equilibrium is employed, which is one of a series of equilibria for code benchmark[8] and is marginally unstable against the ideal ballooning mode, (see Fig.2 in Ref.[20]). The equilibrium pressure p_0, flux-surface averaged equilibrium radial electric field $\langle E_{r0}\rangle_S = -\langle \partial_r \phi_0\rangle_S$, equilibrium parallel current $J_{\parallel 0}$ on the outer mid-plane as well as safety factor q over the radial domain labeled with ψ are shown in Fig. 1 , where $\langle f\rangle_S$ represents the flux-surface averaged value of f, $\partial_r f = B_p R \partial_\psi f$ is the derivative of f with the geometrical radial label, B_p is the poloidal magnetic field, ψ is the poloidal magnetic flux function respectively. Here, physical quantities have been normalized with $R_{\rm ax} = 3.5$ [m], $B_{\rm ax} = 2.0$ [T], $n_i = 1.0 \times 10^{19}$ [m^{-3}] and the deuterium mass. The last closed flux surface or $\psi = 1.0$ is defined as the flux surface where p_0 and $J_{\parallel 0}$ are set to zero.

For tokamak edge simulations, BOUT++ employs the quasi-ballooning coordinate system[9] (ψ, y, z), where ψ is the radial label, y is the parallel label and z is the binormal label respectively. An $1/5$-th of annular wedge torus grid with the radial grid points $N_\psi = 1536$, the parallel grid points $N_y = 64$ and the binormal grid points $N_z = 128$ is employed for nonlinear pedestal collapse simulations. It should be noted that the fine radial grid is required to resolve fine filament structures of perturbed vorticity ϖ_1 and perturbed parallel current $J_{\parallel 1}$ generated by the energy cascade during the pedestal collapse.

A lowpass filter is set at the 32nd harmonics in the binormal direction to avoid aliasing error in the pseudo-spectral method for nonlinear Poisson brackets, which is the well-known as $2/3$-rule[21]. We therefore take $n = 0, 5, 10, \cdots 160$ modes into account, where high-n modes are introduced as an energy sink for energy cascade during the pedestal collapse. The radial boundary conditions used are $\partial_\psi \varpi_1 = 0$, $\partial_\psi p_1 = 0$, $\partial_\psi A_{\parallel 1} = 0$, $\partial_\psi v_{\parallel 1} = 0$,$\partial_\psi \phi_1 = 0$ and $\partial_\psi J_{\parallel 1} = 0$ on the inner radial boundary at $\psi = 0.4$ and $\varpi_1 = 0$, $p_1 = 0$, $\nabla^2_\perp A_{\parallel 1} = 0$, $v_{\parallel 1} = 0$, $\phi_1 = 0$ and $J_{\parallel 1} = 0$ on the outer radial boundary at $\psi = 1.2$ respectively.

3 | SIMULATION RESULTS

In this section, an impact of the equilibrium radial electric field on energy loss processes is investigated by comparing pedestal collapse simulations without and with the equilibrium radial electric field shown in Fig.1 (a). Here, we set the normalized resistivities to $\eta = 10^{-8}$ and $\lambda = 10^{-12}$ and the normalized numerical dissipations to $\mu_\perp = \chi_\perp = \nu_\perp = 10^{-7}$ and $\mu_\parallel = \chi_\parallel = 10^{-1}$ for numerical stability. The linear stability against the resistive ballooning mode (RBM) instability described by Eqs.(1)-(4) with the above parameter set and without equilibrium radial electric field has been tested in Ref.[20] and is summarized again in Fig.2 (a) and (b) with red colored symbols, where ω_A is the poloidal Alfvén frequency. In this case, RBM is stabilized mainly by ion diamagnetism. On the other hand, the equilibrium radial electric field rotates the plasma in the electron diamagnetic direction $\omega > 0$ more strongly and stabilizes RBM more strongly, which is summarized in Fig.2 (a) and (b) with blue colored symbols. In other words, the mean $E \times B$ shearing rate $\omega_{E\times B0} = \langle (R^2 B_p^2/B_0)\partial_\psi (E_{r0}/(B_p R))\rangle_S$ makes the plasma more stable.

As a starting point for discussion on the impact of equilibrium radial electric field on energy loss process after the pedestal collapse, we briefly report the impact of $n = 0$ net flow and $n = 0$ magnetic field generation on energy loss levels in both

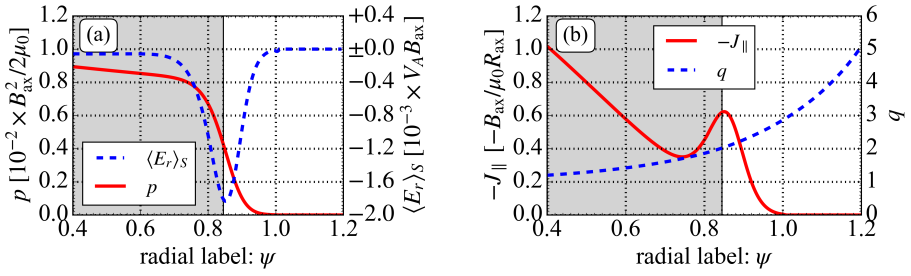

FIGURE 1 Shifted circular equilibrium profiles: (a) pressure (red solid) and flux-surface averaged radial electric field (blue dashed) and (b) parallel current on the outer mid-plane (red solid) and safety factor (blue dashed).

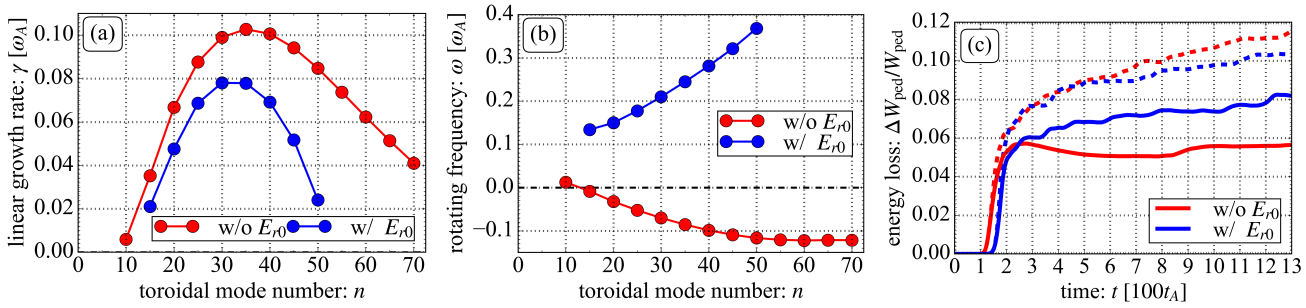

FIGURE 2 (a): linear growth rate versus toroidal mode number in the case without (red) and with (blue) equilibrium radial electric field, (b): plasma rotating frequency versus toroidal mode number in the case without (red) and with (blue) equilibrium radial electric field, (c): time evolution of energy loss level $\Delta W_{\rm ped}/W_{\rm ped}$ in the case without (red) and with (blue) equilibrium radial electric field, where the dashed curves are energy losses assuming $F_1^{n=0}=0$ and $A_{\parallel 1}^{n=0}=0$ and the solid curves are those with $F_1^{n=0}$ and $A_{\parallel 1}^{n=0}$ generations respectively.

simulations with and without equilibrium radial electric field. For this purpose, energy loss levels in pedestal collapse simulations without $n=0$ net flow and $n=0$ magnetic field generation[10,11] are plotted with the dashed curves in Fig 2 (c) as well as those with $n=0$ net flow and $n=0$ magnetic field generation are also plotted with the solid curves in Fig 2 (c). The energy loss level $\Delta W_{\rm ped}/W_{\rm ped}$ is defined as a ratio of released energy $\Delta W_{\rm ped}=\int_{V_{\rm ped}} p_1 dV$ to the energy $W_{\rm ped}=\int_{V_{\rm ped}} p_0 dV$ stored in $0.4\le\psi\le 0.856$ corresponding to the shaded area in Fig. 1 . Here, $\psi=0.856$ is the position where the equilibrium pressure gradient takes the maximum value.

In the simulations without $n=0$ net flow and magnetic field generation, CCs do not transport the $n=0$ perturbed pressure for $\phi_1^{n=0}=-\delta_i p_1^{n=0}$. The energy loss level is therefore determined mainly by the non-local transport described by the nonlinear coupling with $\phi_1^{n=n'}$ and $p_1^{n=-n'}$ in the $E\times B$ convection $-[\phi_1^{n=n'},p_1^{n=-n'}]$ for $n'\neq 0$. There are therefore little differences in the energy loss levels but the timing of pedestal collapse by the early nonlinear phase $t<600t_A$. On the other hand, in the simulations with $n=0$ net flow and $n=0$ magnetic field generation, the equilibrium radial electric field gives a clear difference in energy loss level after the pedestal collapse $t>200t_A$.

In the simulation without the equilibrium radial electric field shown with the red solid curve in Fig 2 (c), the energy loss level decreases due to the partial recovery of pressure profile by $E\times B$ convection by CCs and then increases by the non-local transport triggered by the secondary instability accompanied with damped oscillations[20]. In the simulation with equilibrium radial electric field shown with the blue solid curve in Fig 2 (c), on the other hand, the energy loss level increases after the pedestal collapse and its amplitude is larger than that in the simulation without equilibrium radial electric field although the equilibrium radial electric field stabilizes the RBM as is shown in Fig. 2 (a).

It should be noted that the energy loss level also decreases by $n=0$ net flow and magnetic field generation in the simulation with the equilibrium radial electric field. From the next section, the mechanism increasing the energy loss level after the pedestal collapse in the case with equilibrium radial electric field is investigated.

3.1 | Impact of equilibrium radial electric field on $n=0$ net flow generation and perpendicular flow fluctuations after the pedestal collapse

The energy loss level is highly related with the interaction among CCs and $E\times B$ fluctuations. The radial electric field shear due to ZFs generation suppresses turbulence and the poloidal asymmetric component of CCs gives radial transport of $n=0$ perturbed pressure $p_1^{n=0}$. It is therefore useful to investigate the relation among energy loss level $\Delta W_{\rm ped}/W_{\rm ped}$, the toroidal power spectrum of the perpendicular kinetic energy $W_k^{n=n'}$., and generation mechanism of $n=0$ perpendicular flow. Hereafter, all figures show results including $n=0$ net flow and magnetic field generation.

The time evolution of energy loss and the toroidal mode spectrum of perpendicular kinetic energy W_k are summarized in Fig. 3 . $n=0$ perpendicular kinetic energy or $n=0$ net flow is strongly generated by the energy inflow from the resonant ($n\neq 0$) modes during the pedestal collapse ($t\sim 200t_A$) in both simulations. Subsequent small energy cascades and their resultant energy loss however occur more frequently in the simulation with equilibrium radial electric field while the small energy cascade occurs

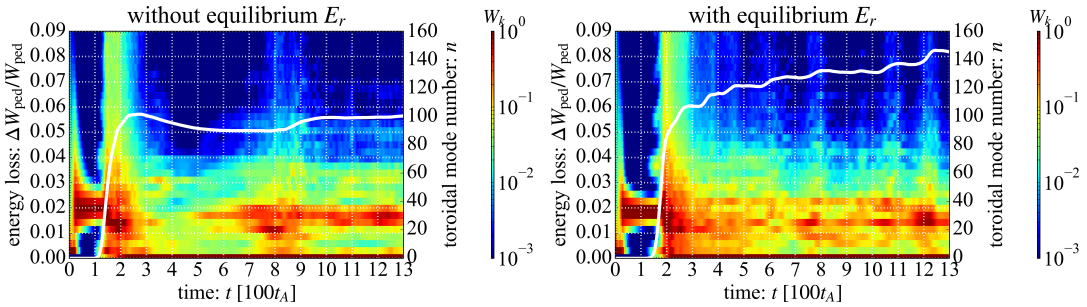

FIGURE 3 Time evolution of energy loss level $\Delta W_{\rm ped}/W_{\rm ped}$ (white solid) and that of toroidal mode spectrum of perpendicular kinetic energy W_k (color map) in the simulation without (left) and with (right) equilibrium radial electric field respectively. Here $W_k^{n=n'}$ has been normalized to set its maximum amplitude unity at every time step.

once at $t \sim 800t_A$ in the simulation without equilibrium radial electric field. The activity of $n \neq 0$ modes of perpendicular kinetic energy also affects the $n = 0$ net flow generation after the pedestal collapse via Reynolds stress and ion diamagnetic flow stress.

Figure 4 summarizes the time evolution of change rate of $n = 0$ perpendicular kinetic energy $W_k^{n=0}$ described in Eq. (5) in the simulation without and with equilibrium radial electric field respectively. During the pedestal collapse, the line-bending term $T_{k,LB}^{n=0}$ is strongly generated to balance with the toroidal curvature term $T_{k,C}^{n=0}$ in both simulations, which means that $n = 0$ magnetic field or $J \times B$ force is generated to balance with the pressure deformation during the pedestal collapse[20,22].

On the other hand, the time evolution of change rate of $n = 0$ perpendicular kinetic energy after the pedestal collapse is qualitatively different between two simulations. The contributions from Reynolds stress and ion diamagnetic flow stress to $n = 0$ perpendicular kinetic energy $W_k^{n=0}$ have peaks corresponding to small energy inverse cascades from unstable modes periodically in the simulation with equilibrium radial electric field. On the other hand, they have a small peak at $t \sim 800t_A$ in the simulation without equilibrium radial electric field.

To clarify this difference, the time evolution of the residual of MHD force balance $T_{k,\text{MHD force}}^{n=0} = T_{k,LB}^{n=0} + T_{k,K}^{n=0} + T_{k,M}^{n=0} + T_{k,C}^{n=0}$ and that of flow stress $T_{k,\text{flow stress}}^{n=0} = T_{k,R}^{n=0} + T_{k,ID}^{n=0}$ after the pedestal collapse are plotted with the change rate of $W_{n=0}^k$ in Fig. 5 . It is clear that the contribution from the residual of flow stress is comparable to that from the residual of MHD force in the simulation with equilibrium radial electric field, while the contribution from the residual of MHD force is dominant in the simulation without equilibrium radial electric field.

3.2 | Impact of equilibrium radial electric field on spatio-temporal structures of $n = 0$ net flow and turbulence

The analyses reported in the previous sections are based on the quantities integrated over the volume, and the spatio-temporal structure of $n = 0$ net flow and that of turbulence have not been discussed, while it has been shown that the radial electric field shear suppresses turbulence by vortex shearing[13]. We therefore investigate the impact of equilibrium radial electric field on

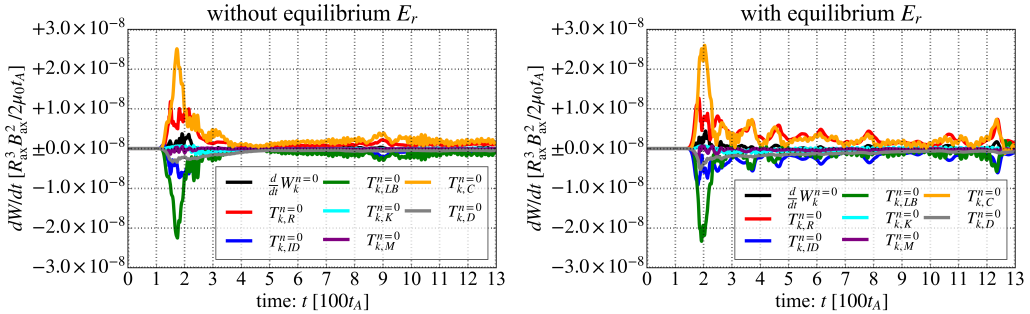

FIGURE 4 Time evolution of breakdown of change rate of the $n = 0$ perpendicular kinetic energy $W_k^{n=0}$ in the case without (left) and with (right) equilibrium radial electric field respectively.

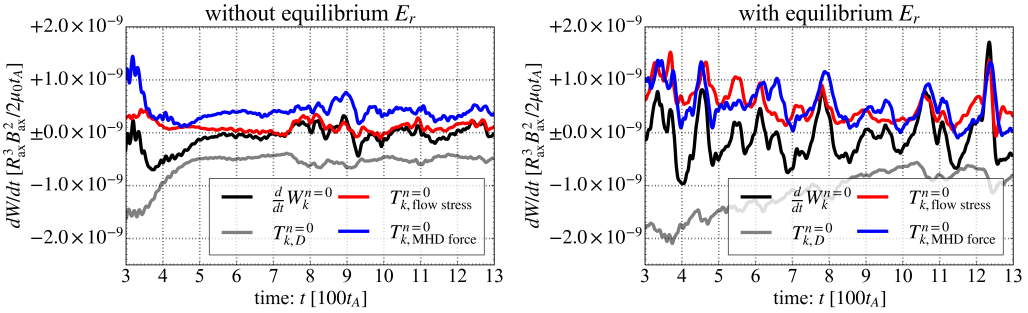

FIGURE 5 Time evolution of the rate of change of $n = 0$ perpendicular kinetic energy (black), dissipation (gray), residual of flow stress (red) and that of MHD force balance (blue) in the simulation without (left) and with (right) equilibrium radial electric field respectively.

the spatio-temporal structure of flux-surface averaged radial electric field $\langle E_r \rangle_S$, pressure gradient $\langle -\partial_r p \rangle_S$, $E \times B$ shearing rate $\omega_{E\times B} = \langle (R^2 B_p^2/B_0)\partial_\psi (E_r/(B_p R)) \rangle_S$ and turbulence intensity $S = [\sum_{m'} \sum_{n' \neq 0} |\phi^{m=m',n=n'}|^2]^{0.5}$, which is summarized in Fig. 6 .

The deep well of the equilibrium radial electric field partially cancels the strong hill of fluctuation driven radial electric field $\langle E_{r1}^{n=0} \rangle_S$ after the pedestal collapse in the simulation with equilibrium radial electric field, which decreases the $E \times B$ shearing rate intensity $|\omega_{E\times B}|$ or the turbulence suppression by vortex shearing. The spatio-temporal structure of turbulence intensity becomes more bursty and the non-local energy transport increases if the equilibrium radial electric field is taken into account. This is the reason why subsequent small energy cascades occur more frequently in the toroidal mode spectrum of perpendicular kinetic energy in the simulation with equilibrium radial electric field.

Our previous work[20] based on simulations without equilibrium radial electric field indicates that the subsequent turbulence bursts can be triggered by a pressure-driven damped oscillation[23] where the pressure gradient is prey and the turbulence is the predator. This is a kind of electromagnetic nonlinear cycle in order of the pressure gradient, the flow shear and the turbulence in the left of Fig. 7 while the turbulence changes in prior to the ZFs in the electrostatic turbulence-driven oscillation[24]. The phase diagram analysis in the right of Fig. 7 indicates that the subsequent small turbulence bursts in the simulation with equilibrium radial electric field is also triggered the pressure-driven oscillation although the contribution from the residual of

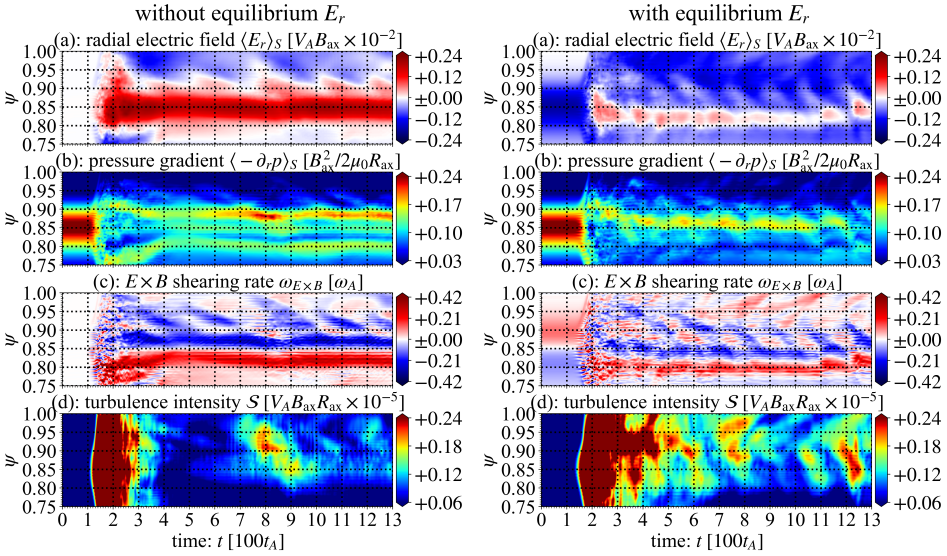

FIGURE 6 Spatio-temporal structure of (a) flux-surface averaged radial electric field $\langle E_r \rangle_S$, (b) flux-surface averaged pressure gradient $\langle -\partial_r p \rangle_S$, (c) $E \times B$ shearing rate $\omega_{E\times B}$ and (d) turbulence intensity S in the simulation without (left) and with (right) equilibrium radial electric field respectively.

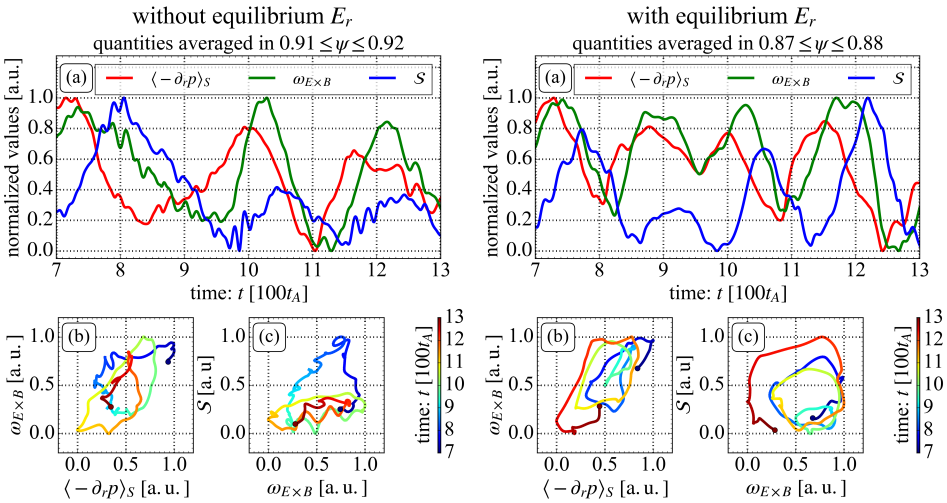

FIGURE 7 (a) time evolution of pressure gradient $\langle -\partial_r p \rangle_S$ (red), $E \times B$ shearing rate $\omega_{E\times B}$ (blue) and turbulence intensity S, (b) Lissajous diagram between pressure gradient and $E \times B$ shearing rate and (c) Lissajous diagram between $E \times B$ shearing rate and turbulence intensity in the case without (left) and with (right) equilibrium radial electric field respectively.

flow stress to $n = 0$ net flow generation is comparable with that from the residual of MHD force balance. It should be noted that subsequent turbulence bursts by pressure-driven nonlinear oscillation might be a possible mechanism of compound ELMs like the subsequent collapse reported in Ref. [16]. Further analyses including validation of the simulation results with compound ELM experiments are required, which is left for a future work.

4 | SUMMARY

In summary, an impact of equilibrium radial electric field on energy loss processes has been numerically investigated by comparing the simulations without and with equilibrium radial electric field. According to the temporal-spatio analyses, the deep well of the equilibrium radial electric field partially cancels the strong hill formation by the fluctuation driven radial electric field after the pedestal collapse, which decreases the $E \times B$ shearing rate intensity. This increases energy loss by subsequent turbulence bursts while the equilibrium radial electric field stabilizes RBM in the linear phase. The energy transfer rate analysis has shown that the equilibrium radial electric field increases the contribution from residual of flow stresses to $n = 0$ perpendicular kinetic energy to be comparable to that from the MHD force balance. The phase diagram analysis however has shown that the subsequent turbulent bursts is also driven by the pressure-gradient driven nonlinear oscillation in the simulation with equilibrium radial electric field.

Acknowledgments

This work was partially supported by JSPS KAKENHI Grant No. 16K18342 and was performed under the auspices of the U.S. Department of Energy by Lawrence Livermore National Laboratory under Contract No. DE-AC52-07NA27344. Computations were carried out on JFRS-1 supercomputer at Computational Simulation Centre of International Fusion Research Centre.

References

[1] F Wagner, G Becker, K Behringer, D Campbell, A Eberhagen, W Engelhardt, G Fussmann, O Gehre, J Gernhardt, G v Gierke, G Haas, M Huang, F Karger, M Keilhacker, O Klüber, M Kornherr, K Lackner, G Lisitano, G G Lister, H M Mayer, D Meisel, E R Müller, H Murmann, H Niedermeyer, W Poschenrieder, H Rapp, H Röhr, F Schneider, G Siller, E Speth, A Stäbler, K H Steuer, G Venus, O Vollmer, Z Yü, *Physical Review Letters* **1982**, *49* (19), 1408–1412.

[2] A Loarte, B Lipschultz, A S Kukushkin, G F Matthews, P C Stangeby, N Asakura, G F Counsell, G Federici, A Kallenbach, K Krieger, A Mahdavi, V Philipps, D Reiter, J Roth, J Strachan, D Whyte, R Doerner, T Eich, W Fundamenski, A Herrmann, M Fenstermacher, P Ghendrih, M Groth, A Kirschner, S Konoshima, B LaBombard, P Lang, A W Leonard, P Monier-Garbet, R Neu, H Pacher, B Pegourie, R A Pitts, S Takamura, J Terry, E Tsitrone, the ITPA Scrape-off Layer Group, Diver, *Nuclear Fusion* **2007**, *47* (6), S203–S263.

[3] N Asakura, K Hoshino, S Suzuki, S Tokunaga, Y Someya, H Utoh, H Kudo, Y Sakamoto, R Hiwatari, K Tobita, K Shimizu, K Ezato, Y Seki, N Ohno, Y Ueda, Joint Special Team for DEMO Design, *Nuclear Fusion* **2017**, *57* (12), 126050–13.

[4] H Zohm, *Plasma Physics and Controlled Fusion* **1996**, *38* (8), 1213–1223.

[5] G T A Huysmans, O Czarny, *Nuclear Fusion* **2007**, *47* (7), 659–666.

[6] O Czarny, G Huysmans, *Journal of Computational Physics* **2008**, *227* (16), 7423–7445.

[7] A Y Pankin, G Bateman, D P Brennan, A H Kritz, S Kruger, P B Snyder, C Sovinec, the NIMROD team, *Plasma Physics and Controlled Fusion* **2007**, *49* (7), S63.

[8] N M Ferraro, S C Jardin, P B Snyder, *Physics of Plasmas* **2010**, *17* (10), 102508–11.

[9] B D Dudson, M V Umansky, X Q Xu, P B Snyder, H R Wilson, *Computer Physics Communications* **2009**, *180* (9), 1467–1480.

[10] X Q Xu, B Dudson, P B Snyder, M V Umansky, H Wilson, *Physical Review Letters* **2010**, *105* (17), 949–4.

[11] B D Dudson, X Q Xu, M V Umansky, H R Wilson, P B Snyder, *Plasma Physics and Controlled Fusion* **2011**, *53* (5), 054005–14.

[12] R. Z. Sagdeev, V. D. Shapiro, V. I. Shevchenko, *Soviet Journal of Plasma Physics* **1978**, *4*, 551–559.

[13] P H Diamond, S I Itoh, K Itoh, T S Hahm, *Plasma Physics and Controlled Fusion* **2005**, *47* (5), R35–R161.

[14] T S Hahm, K H Burrell, *Physics of Plasmas* **1995**, *2* (5), 1648–1651.

[15] K H Burrell, *Physics of Plasmas* **1997**, *4* (5), 1499–1518.

[16] Hogun Jhang, Helen H Kaang, S S Kim, T Rhee, R Singh, T S Hahm, *Nuclear Fusion* **2017**, *57* (2), 022006–10.

[17] N Winsor, J L Johnson, J M Dawson, *Physics of Fluids* **1968**, *11* (11), 2448–2450.

[18] R Sartori, G Saibene, L D Horton, M Becoulet, R Budny, D Borba, A Chankin, G D Conway, G Cordey, D McDonald, K Guenther, M G von Hellermann, Yu Igithkanov, A Loarte, P J Lomas, O Pogutse, J Rapp, *Plasma Physics and Controlled Fusion* **2004**, *46* (5), 723–750.

[19] B D Dudson, J Leddy, *Plasma Physics and Controlled Fusion* **2017**, *59* (5), 054010–13.

[20] H Seto, X Q Xu, B D Dudson, M Yagi, *Physics of Plasmas* **2019**, *26* (5), 052507–16.

[21] S A Orszag, *Journal of the Atmospheric Sciences* **1971**, *28*, 1074.

[22] G T A Huysmans, S Pamela, E van der Plas, P Ramet, *Plasma Physics and Controlled Fusion* **2009**, *51* (12), 124012–15.

[23] J Cheng, J Q Dong, K Itoh, L W Yan, M Xu, K J Zhao, W Y Hong, Z H Huang, X Q Ji, W L Zhong, D L Yu, S I Itoh, L Nie, D F Kong, T Lan, A D Liu, X L Zou, Q W Yang, X T Ding, X R Duan, Yong Liu, *Physical Review Letters* **2013**, *110* (26), 265002–5.

[24] E J Kim, P H Diamond, *Physical Review Letters* **2003**, *90* (18), 313–4.

How to cite this article: Seto H., Xu X.Q., Dudson B.D., and Yagi M. (20xx), Simulation study on impact of equilibrium radial electric field on energy loss process after pedestal collapse, *Q.J.R. Meteorol. Soc.*, *2017;00:1–6*.